

# Fast Acquisition Protocol for X-ray Scattering Tensor Tomography

**Jisoo Kim**

University and ETH Zurich

**Matias Kagias** (✉ [mkagias@caltech.edu](mailto:mkagias@caltech.edu))

Paul Scherrer Institute

**Federica Marone**

Paul Scherrer Institute

**Zhitian Shi**

University and ETH Zurich

**Marco Stampanoni**

University and ETH Zurich

---

## Research Article

**Keywords:** Fast acquisition protocol, X-ray scattering tensor, tomography, Microstructural information, sample

**Posted Date:** June 10th, 2021

**DOI:** <https://doi.org/10.21203/rs.3.rs-599550/v1>

**License:**   This work is licensed under a Creative Commons Attribution 4.0 International License.

[Read Full License](#)

---

**Version of Record:** A version of this preprint was published at Scientific Reports on November 29th, 2021. See the published version at <https://doi.org/10.1038/s41598-021-02467-w>.

# Fast acquisition protocol for X-ray scattering tensor tomography

Jisoo Kim<sup>1,2</sup>, Matias Kagias<sup>2,\*</sup>, Federica Marone<sup>2,\*</sup>, Zhitian Shi<sup>1,2</sup>, and Marco Stampanoni<sup>1,2</sup>

<sup>1</sup>Institute for Biomedical Engineering, University and ETH Zürich, 8092 Zürich, Switzerland

<sup>2</sup>Swiss Light Source, Paul Scherrer Institut, 5232 Villigen, Switzerland

\*mkagias@caltech.edu; federica.marone@psi.ch

†Currently at the Division of Engineering and Applied Science, California Institute of Technology, Pasadena, CA 91125, USA

## ABSTRACT

Microstructural information over an entire sample is important to understand the macroscopic behavior of materials. X-ray scattering tensor tomography facilitates the investigation of the microstructural organisation in statistically large sample volumes. However, established acquisition protocols based on scanning small-angle X-ray scattering and X-ray grating interferometry inherently require long scan times even with highly brilliant X-ray sources. Recent developments in X-ray diffractive optics towards circular pattern arrays enable fast single-shot acquisition of the sample scattering properties with 2D omnidirectional sensitivity. Leveraging on these new optical elements, we propose here simple yet inherently rapid acquisition protocols for X-ray scattering tensor tomography. Results from both simulation and experimental data, supported by a null space analysis, suggest that the proposed acquisition protocols are not only rapid but also corroborate that sufficient information for the accurate volumetric reconstruction of the scattering properties is provided. The proposed acquisition protocols will build the basis for rapid inspection and/or time-resolved tensor tomography of the microstructural organisation over an extended field of view.

## 1 Introduction

The micro- and nano-structure of various natural and artificial materials is at the base of their macroscopic properties. For instance, the local orientation of collagen fibres is strongly related to the mechanical properties of bone<sup>1,2</sup> and the local orientation of neuronal axons determines the structural and functional network of the brain<sup>3</sup>. Likewise for synthetic fibre based materials, their mechanical, thermal and electrical properties<sup>4-6</sup> are dictated by the local fibre orientation as well as by how well the fibres are aligned. The possibility to investigate the microscopic architecture in statistically large enough sample volumes would therefore be valuable during the development of new materials as well as for quality control in industrial settings.

X-rays are useful to obtain information on the inner structure of materials in a non-destructive manner. However, in conventional X-ray imaging, just like in many other modalities, a trade-off between spatial resolution and examined field of view (FOV) is unavoidable. With an effective detector pixel size of a few  $\mu\text{m}$  and a few thousands detector pixels, the FOV is limited to a few mm. Small-angle X-ray scattering contrast can mitigate the trade-off between the length-scale of interest and the FOV, facilitating full correlative studies of the micro- and nano-structure over macroscopic sample volumes<sup>7-9</sup>. With X-ray scattering tensor tomography, a set of coefficients of the scattering tensor which models the 3D scattering distribution of the underlying microstructure can be reconstructed in each voxel<sup>10,11</sup>. The acquisition setup needs though to be equipped with three angular degrees of freedom to provide the necessary information. This is because anisotropic structures cause anisotropic scattering and the probed signal depends on the relative orientation between the underlying structure and the incident beam<sup>12</sup>. These requirements typically lead to acquisition times in the order of several hours hindering any large (cm) scale exploitation of scattering tensor tomography<sup>10,13</sup>.

Circular gratings arranged in an array can provide scattering information in multiple directions in a single shot<sup>14,15</sup>, hence reducing the required angular degrees of freedom to two. We have previously demonstrated X-ray scattering tensor tomography with the use of this circular grating array<sup>16</sup>, with which the reduction in acquisition time is considerable compared to pre-existing techniques<sup>10,17</sup> owing to the omnidirectional scattering sensitivity of the used diffractive optical component. To take full advantage of this circular grating array and push the acquisition speed as well as minimize acquisition overhead, different acquisition protocols have to be assessed and investigated. In this paper, we propose rapid acquisition protocols relying on a setup with two rotational axes and the recently developed circular grating array (or potentially any other method

37 providing omnidirectional scattering sensitivity<sup>18,19</sup>). By accelerating the data acquisition, more time-efficient inspection of the  
38 microstructure organisation over an extended FOV will be enabled, making this technology attractive for industrial applications.  
39 Moreover, the proposed rapid acquisition protocols with minimal acquisition overhead coupled with bright X-ray sources will  
40 unlock time-resolved X-ray scattering tensor tomography capabilities.

41 In order to assess and compare the performance of different acquisition protocols, we first performed a null space analysis  
42 to investigate the intrinsic characteristics of the different acquisition geometries. In a second step, simulation studies are used to  
43 validate the acquisition protocols independently from any possible experimental deviations such as sample misalignment and  
44 motor inaccuracies. Experimental studies were finally carried out to test the robustness and confirm the performance of the  
45 proposed acquisition protocols also under real investigation conditions.

## 46 2 Methods

### 47 2.1 X-ray scattering tensor tomography with circular gratings

48 A schematic overview of the experimental setup for X-ray scattering tensor tomography with circular gratings is shown in  
49 Fig. 1. In order to capture 2D-omnidirectional X-ray scattering signals with a single X-ray projection, a periodic array of  
50 multi-circular gratings based on a diffractive annular structure is used in this study<sup>15</sup>. This diffractive structure is characterized  
51 by a global period  $P$  which is half the repetition period of the unit cell and by  $g$  which is the period of the fine circular gratings  
52 within each unit cell as shown in Fig. 1b. The etching depth of the gratings is dependent on the wavelength  $\lambda$  of the used  
53 X-rays and design phase shift. More details regarding the grating design and fabrication can be found in the reference<sup>15,20</sup>.  
54 The circular grating array is placed at a distance  $L = Pg/2\lambda$  upstream from the detector as shown in Fig. 1a. The circular  
55 diffraction fringe formed at the detector position is readout by multiple detector pixels and an exemplary unit cell window of  
56  $9 \times 9$  pixels is shown in Fig. 1c. The directional scattering signal is extracted from the fringes along different signal extraction  
57 angles  $\gamma$ . For all studies with the use of circular grating array in this paper, the scattering signal extraction angle  $\gamma$  was set to be  
58  $\{-90^\circ, -67.5^\circ, \dots, 67.5^\circ\}$ . The directional scattering signals are collected from projections acquired with the sample positioned  
59 at different angles  $\alpha$  and  $\beta$  and the projection vector  $\mathbf{p}$  is formed. The angle  $\alpha$  and  $\beta$  represent the rotation and tilt of the stage  
60 as shown in Fig. 1a. For each voxel in the vectorized reconstruction volume  $\boldsymbol{\mu}$ , the scattering distribution is sampled along  $k$   
61 different scattering sampling directions. We used seven scattering sampling direction vectors  $\mathbf{S}_k$  (three directions parallel to the  
62 x, y, and z axes and four diagonal directions). To recover the unknown  $\boldsymbol{\mu}$ , the system of linear equations  $\mathbf{p} = A\boldsymbol{\mu}$  is solved.  $A$   
63 is the system matrix computed as a multiplication of the scaling matrix for different scattering sampling directions and the  
64 geometric system matrix for discrete beam path integrals. Principal component analysis (PCA) is applied to the reconstructed  
65 scattering distribution  $\boldsymbol{\mu}$  which is modeled with an ellipsoid approximation: three principal axes are computed for each voxel.  
66 The principal axis with the shortest length represents the main scattering orientation, the mean length of the three principal axes  
67 the average scattering intensity, and the fractional anisotropy<sup>21</sup> the degree of scattering anisotropy. Detailed information on the  
68 signal extraction and tensor reconstruction methods used in this study can be found in the following reference works<sup>15-17,22</sup>.

### 69 2.2 Acquisition protocols

70 In general, acquisition protocols which widely and densely cover a virtual unit sphere around samples provide more accurate  
71 tensor reconstruction results. It is possible to design optimized but rather complicated trajectories to cover a certain number of  
72 scattering orientations, if conventional linear gratings are used<sup>13</sup>. Those complicated trajectories result in a larger acquisition  
73 overhead and are not ideal for rapid tensor tomography acquisition. Here, we implement instead two simple acquisition types -  
74 stairwise and spiral acquisition protocols, based on a simple two-axis system and compatible with a higher acquisition speed  
75 with minimized acquisition overhead. These acquisition protocols rely on the use of circular grating arrays or any other method  
76 with omnidirectional scattering sensitivity such as the speckle pattern based<sup>18</sup> and the scanning small-angle scattering based  
77 methods<sup>10</sup> as well as the recently developed omnidirectional simultaneous reciprocal and real space imaging method<sup>23</sup>.

78 The stairwise acquisition protocols foresee a stepwise tilting of the rotation axis as previously implemented for scanning  
79 SAXS, which has omnidirectional scattering sensitivity<sup>24</sup>. The rotation motor turns from  $\alpha = 0^\circ$  to  $\alpha = 360^\circ$  at each angle  $\beta_i$   
80 from the set of chosen  $n$  tilt angles  $\beta = \{\beta_i | \beta_{min} \leq \beta_i \leq \beta_{max}, i = 1, \dots, n\}$ , resulting in stairwise beam trajectories. The number  
81 of projections at each tilt angle is kept constant in this study. In addition to the stairwise acquisition protocol, we also propose a  
82 spiral acquisition scheme to push the acquisition speed and minimize overhead. The spiral acquisition trajectory is realized  
83 by tilting the rotation axis while the sample is being rotated. The rotation and tilt motors simultaneously turn from  $\alpha = 0^\circ$  to  
84  $\alpha = 360^\circ \times n$  and  $\beta = \beta_{min}$  to  $\beta = \beta_{max}$ . The spiral acquisition provides projection views at more tilt angles than the stairwise  
85 acquisition. The overhead is inherently close to zero for the spiral protocol whereas acquisition overhead in between each tilt  
86 angle is difficult to avoid for the stairwise scheme. For both acquisition types, the maximum tilt angle  $\beta_{max}$  is limited in our  
87 current setup to  $45^\circ$  because the motor stage blocks the beam at larger tilt angles. Beam enter/exit trajectories on a unit sphere  
88 from the sample's point of view for different acquisition protocols are shown in Fig. 2.

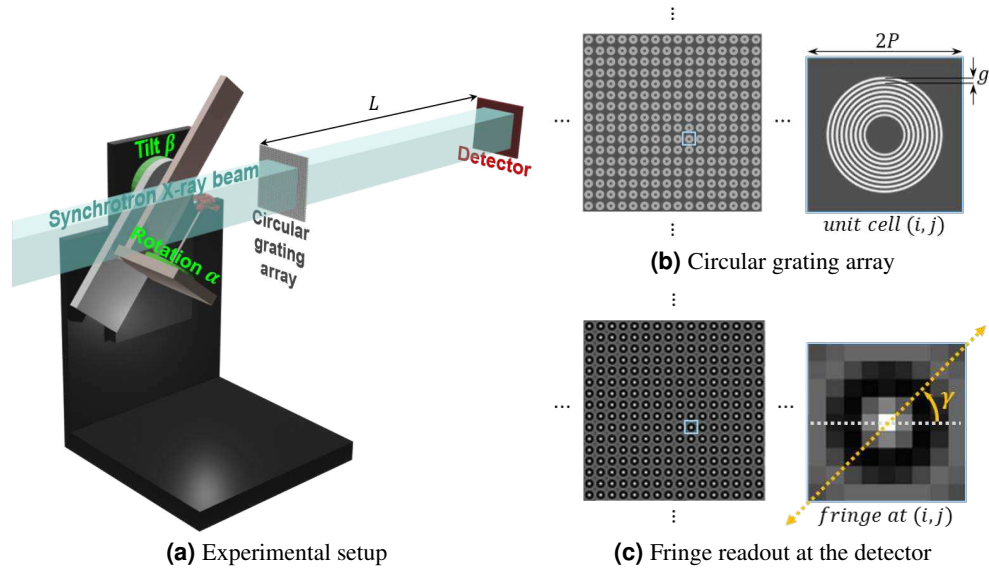


**Figure 1.** Experimental setup for X-ray scattering tensor tomography with circular gratings. An overview of the setup is shown in (a). The rotation motor revolves  $\alpha$  degrees and the rotation axis can be tilted  $\beta$  degrees. The circular grating array (b) is composed of unit cells where  $P$  is half the unit cell size and  $g$  is the period of the fine grating lines. It is placed near the sample at a distance  $L = Pg/2\lambda$  from the detector. A circular fringe (c) is formed at the detector where the 2D directional scattering signal is extracted by measuring the visibility reduction along the radial profile at an angle  $-90^\circ \leq \gamma < 90^\circ$ .

89 The difference in the beam trajectories between the two acquisition types is largest when  $n = 1$ . Acquisitions with  $n = 5$   
 90 and a total of 100 projections show a more uniform distribution of beam enter/exit points over the unit sphere compared to  
 91  $n = 1$  with the same total number of projections. We may expect a better reconstruction accuracy with  $n = 5$  compared to with  
 92  $n = 1$ . However, for a given total acquisition time, the protocol with  $n = 5$  requires a rotation ( $\alpha$ ) speed five times higher than  
 93 for  $n = 1$ . This could lead to increased motion and blurring artifacts especially for time resolved experiments with a short total  
 acquisition time; it could therefore be beneficial to minimize  $n$  in such cases.

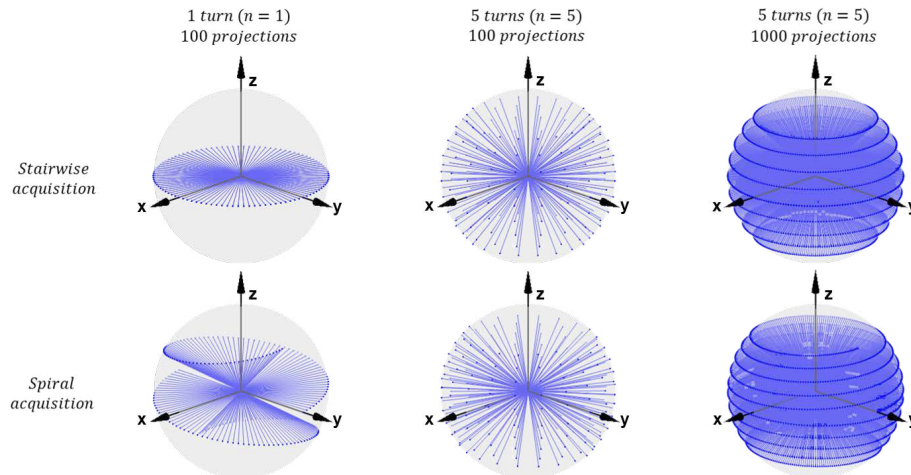


**Figure 2.** Beam enter/exit trajectories for stairwise and spiral acquisition schemes from the sample's point of view. The number of turns  $n$  and the total number of projections are indicated on top of the plots. The tilt angle  $\beta$  for the shown stairwise trajectory with  $n = 1$  is  $0^\circ$  but it can be chosen to be any angle between  $0^\circ$  and  $45^\circ$ .

### 95 2.3 Null space computation

96 The null space is the linear subspace of all vectors  $\boldsymbol{\mu}$  mapped to zero ( $A\boldsymbol{\mu} = \mathbf{0}$ ) and can be derived purely from the system  
 97 matrix  $A$  which describes the geometrical setup of an acquisition protocol. The existence of a non-trivial null space implies  
 98 that certain components in the reconstruction volume cannot be confidently recovered from the measurements; therefore, the  
 99 null space analysis can be used to assess which part of the model can be resolved with a specific acquisition geometry<sup>25</sup>. For  
 100 example a null space analysis was used to evaluate the uncertainty of the computed reconstruction for the isotropic scattering  
 101 component in anisotropic X-ray darkfield tomography (AXDT), with conventional linear gratings<sup>13</sup>.

102 A non-trivial null space  $\boldsymbol{\mu}_{null}$  always exists when the system matrix  $A$  is rank deficient. Any vector  $\boldsymbol{\mu}$  in such a system  
 103 can be decomposed into the minimum-norm least square solution  $\boldsymbol{\mu}_{LS}$  and the null space  $\boldsymbol{\mu}_{null}$  that are orthogonal to each  
 104 other, holding the following property:  $A\boldsymbol{\mu} = A(\boldsymbol{\mu}_{LS} + \boldsymbol{\mu}_{null}) = A\boldsymbol{\mu}_{LS}$ . The computation of the null space based on singular  
 105 value decomposition (SVD) is efficient for small problems. For larger system, such as our tensor tomography problem, the  
 106 high memory requirements of this method prevent its use on the full representation of  $A$ . An iterative method is employed here  
 107 instead: finding the null space is equivalent to solving the following constrained optimisation problem:

$$\min_{\boldsymbol{\mu}_{null}} \frac{1}{2} \|\boldsymbol{\mu}_{null} - \mathbf{v}\|_2^2 \quad \text{subject to} \quad A\boldsymbol{\mu}_{null} = \mathbf{0} \quad (1)$$

108  $\mathbf{v}$  is a random vector whose elements are in the range of  $[0, 1]$ . An approximate solution  $\boldsymbol{\mu}_{null}$  is found by setting the gradient of  
 109 the Lagrange function  $\mathcal{L}(\boldsymbol{\mu}_{null}, \boldsymbol{\lambda})$  of the above problem to zero and iteratively solving it, where  $\boldsymbol{\lambda}$  is the Lagrange multiplier  
 110 vector.

$$\nabla \mathcal{L}(\boldsymbol{\mu}_{null}, \boldsymbol{\lambda}) = \mathbf{0} \quad \Leftrightarrow \quad \begin{bmatrix} I & A^T \\ A & 0 \end{bmatrix} \begin{bmatrix} \boldsymbol{\mu}_{null} \\ \boldsymbol{\lambda} \end{bmatrix} = \begin{bmatrix} \mathbf{v} \\ \mathbf{0} \end{bmatrix} \quad (2)$$

### 111 2.4 Assessment of the reconstruction accuracy

112 To assess and quantify the reconstruction results in scattering tensor tomography, more aspects than in conventional scalar  
 113 tomography need to be taken into account because a single voxel is characterized by more than one parameter. Analogously to  
 114 scalar tomography, the distance between the tensor in each voxel for the reference and the evaluated reconstructed volumes can  
 115 be computed. We use here the inner product of the structure main orientation vectors  $\mathbf{v}_{ref}$  and  $\mathbf{v}$ ,  $I = |\langle \mathbf{v}_{ref}, \mathbf{v} \rangle|$  in each voxel, as  
 116 the error metric to assess the orientation reconstruction accuracy of data acquired with different acquisition protocols, where  
 117  $\mathbf{v}_{ref}$  and  $\mathbf{v}$  are the reconstructed structure orientation vector of the reference and the assessed volume respectively. In addition  
 118 to the error in the reconstructed orientation, we also use an error metric  $E = (s_{ref} - s)^2$  to compare the average or scattering  
 119 anisotropy signal  $s$ , which is a scalar variable, extracted from the reconstructed tensor in each voxel.

## 120 3 Results

### 121 3.1 Null space analysis

122 The null space was computed for different system matrices for different acquisition protocols for an example reconstruction  
 123 volume size of  $50 \times 50 \times 50$  voxels. The total number of projections was fixed to 1000 for all acquisition protocols. The  
 124 computed null space was averaged along the z-direction (parallel to the rotation axis when the tilt angle is zero) for different  
 125 scattering sampling directions and visualized in Fig. 3. The scattering sampling directions should not be confused with the  
 126 structure orientation. High values in the null space indicate that the acquisition protocol provides large uncertainties in the  
 127 reconstruction results. Fig. 3a-3e show that the information for certain scattering sampling directions cannot be reconstructed  
 128 with the conventional linear grating arrays, independently on whether the linear grating array is aligned vertically ( $\gamma = 0^\circ$ ) or  
 129 horizontally ( $\gamma = 90^\circ$ ). The null space is reduced when  $n = 10$  and the linear grating array is aligned horizontally as shown  
 130 in Fig. 3f, even though the null space for  $k = 1, 2$  remains higher compared to the other components. On the other hand, a  
 131 significantly larger reduction in the null space is achieved by using a circular grating array already when  $n = 1$  ( $\beta = 0^\circ$ ) as  
 132 shown in Fig. 3g. Choosing a tilt angle of  $\beta = 22.5^\circ$  instead of  $\beta = 0^\circ$  or using the spiral acquisition protocol instead of the  
 133 stairwise one gives a smaller null space as shown in Fig. 3h, 3j, respectively. We observe a general reduction in the null space  
 134 when  $n$  is increased from 1 to 10 both for the stairwise ( $\beta = \{0^\circ, 5^\circ, \dots, 45^\circ\}$ ) and spiral ( $\beta_{min} = 0^\circ$  and  $\beta_{max} = 45^\circ$ ) acquisition  
 135 geometry. Little difference is observed between the stairwise and spiral acquisition protocols when  $n = 10$  as we can see in  
 136 Fig. 3i, 3k. Summarizing, an improvement in the tensor reconstruction accuracy with a circular grating array even at small  $n$   
 137 compared to the case of linear grating arrays is expected. Also, a better reconstruction accuracy with the spiral acquisition  
 138 protocol should be achieved compared to results with the tilt angle fixed of  $\beta = 0^\circ$ . Instead, comparable results are expected for  
 139 the stairwise protocol with a fixed tilt angle of  $\beta = 22.5^\circ$  and the spiral acquisition with  $n = 1$ .

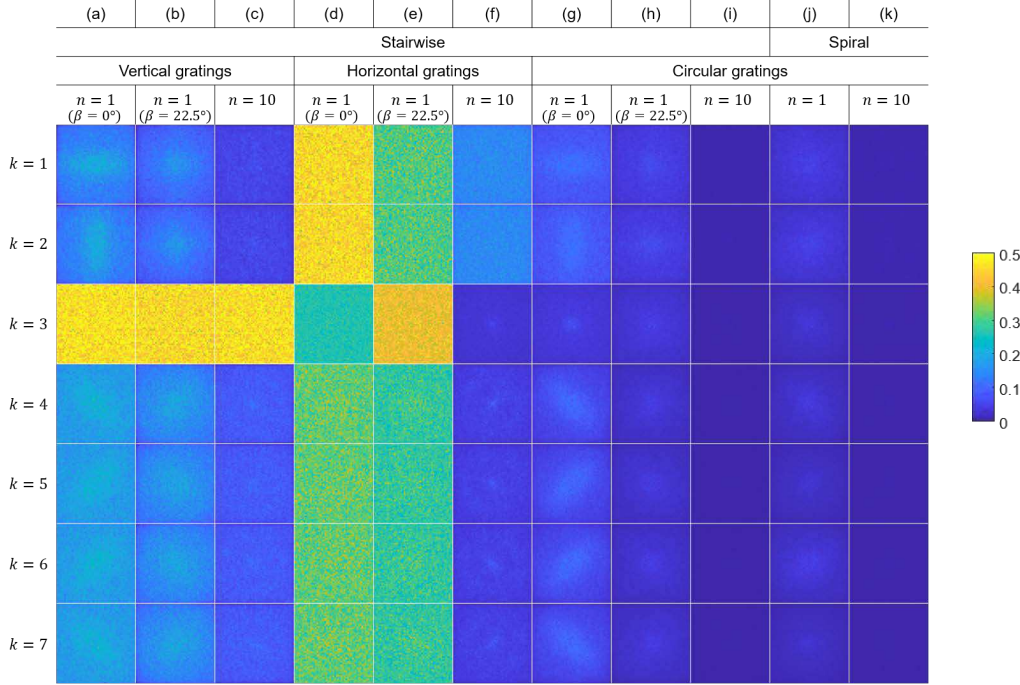


**Figure 3.** Visualisation of the computed null space for different scattering sampling directions  $k$ . The null space was computed for different acquisition geometries: stairwise and spiral acquisition; different grating types: vertically aligned linear gratings, horizontally aligned linear gratings, and circular gratings; different number of turns  $n$ .  $\beta$  indicates the tilt angle. High values in null space for scattering component  $k$  indicate that the acquisition protocol provides large uncertainties in the reconstruction for that component.

### 3.2 Simulation study

In a first step we have assessed the performance of the proposed acquisition protocols by conducting experiments with an *in silico* sample shown in Fig. 4a. The cubic sample is divided into eight equal subvolumes with fibres oriented in different directions as described in Fig. 4b. The preferential fibre orientation in each voxel is color coded with the [R,G,B] values corresponding to the absolute values of the components [x,y,z] of the vector representing the fibre direction. The corresponding color mapping sphere is shown in Fig. 4c. This color coding scheme for the visualisation of 3D orientations is used throughout this paper. The reference volume  $\boldsymbol{\mu}_{k,ref}$  was generated by calculating the squared inner product of the scattering sampling directions and the fibre orientation  $|\langle \mathbf{S}_k, \mathbf{o}_{fibre} \rangle|^2$ . System matrices for different acquisition geometries were computed. Projection data were generated by forward projection of the reference volume using these system matrices rather than by simulating individual fibres and using a wave propagation approach, since the accuracy of the current simulation setup should be sufficient for the purpose of this study. Additive zero-mean white Gaussian noise proportional to the absorption signal was added to the simulated projections. This is a valid approximation assuming a high-flux environment<sup>26</sup>.

Projection images were computed for different angular positions with  $n$  from 1 to 7 both for the stairwise and the spiral acquisition geometries. The total number of projections was fixed to 1000. Axial slices through the reconstructed volumes are shown in Fig. 4 for  $n = 1, 3, 7$ . Ideally in this simulation study, the average scattering and scattering anisotropy should have the same value in every voxel for subvolumes 1 to 7. As predicted from the null space analysis, the largest deviations from the reference volume are observed for  $n = 1$  with a fixed tilt angle of  $\beta = 0^\circ$ . The reconstruction for  $\beta = 22.5^\circ$ ,  $n = 1$  and the stairwise acquisition looks closer to the reference than the  $\beta = 0^\circ$  case. Reconstructions for all  $n$  and the spiral acquisition protocol look instead fairly similar, with larger variations in the average scattering and scattering anisotropy. For  $n \geq 3$ , the reconstruction results for the stairwise and spiral acquisition geometries are comparable. For a more quantitative assessment of the reconstruction results, the inner product  $I$  of the reconstructed orientation vectors with the ground truth reference vectors was calculated for all voxels of the different subvolumes and the results are shown in the form of box plots in Fig. 5a. For the stairwise acquisition protocol, the largest inaccuracy is observed for  $n = 1$  for subvolume 1 and 2 where the fibres lie in the horizontal (x-y) plane as could already be visually appreciated in Fig. 4d. In Fig. 5a, we observed a larger orientation inaccuracy when  $n = 1$  for subvolume 7 with diagonally oriented fibres compared to other subvolumes with diagonally oriented fibres. This observation arises from the fact that the directional scattering information in subvolume 7 is contaminated by

166 signals from the neighbor subvolumes 1 and 2, where the fibres aligned in the xy-plane scatter isotropically in a certain angular  
 167 range of projection. It means that the reconstruction accuracy depends not only on the acquisition scheme but also on the  
 168 surrounding structures around the region of interest. The inner product  $I$  approaches 1 when  $n \geq 3$  for all subvolumes. For the  
 169 spiral acquisition geometry, only minor variations in the inner product  $I$  for different  $n$  and subvolumes exist. For the error  $E$   
 170 analysis of the average scattering and scattering anisotropy results (Fig. 5b, 5c), the subvolumes were grouped into non-empty  
 171 (1-7) and empty (8). In general, the error  $E$  for both the average scattering and scattering anisotropy signal was larger in the  
 172 empty subvolume, but no significant difference in error  $E$  is observed for different  $n$  and geometries except for  $n = 1$  and the  
 173 stairwise acquisition protocol. In addition, the inner product  $I$  and the error  $E$  were similar for a fixed tilt angled of  $\beta = 22.5^\circ$   
 174 and the spiral acquisition when  $n = 1$  as predicted by the null space analysis (Fig. 3h and 3j).

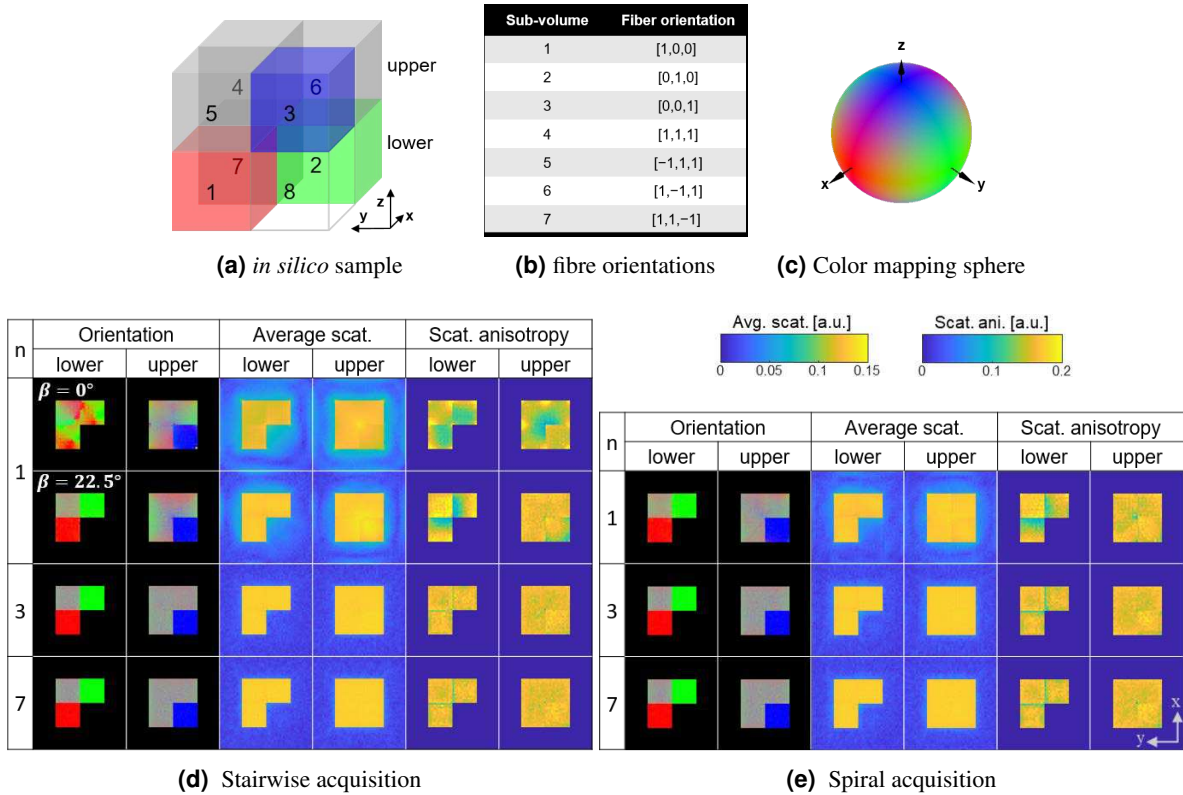
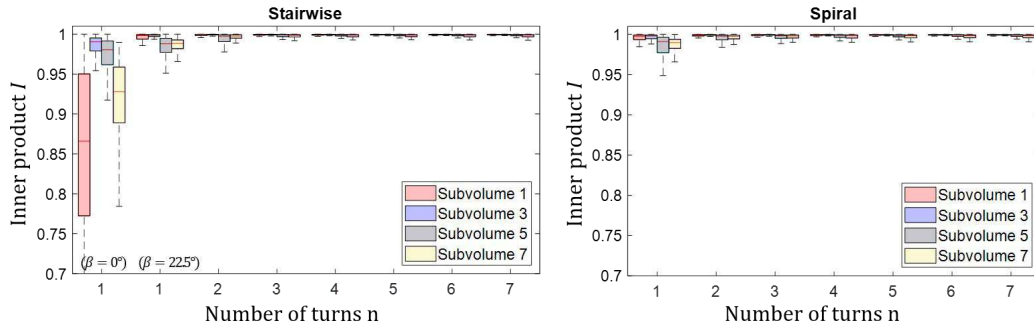


**Figure 4.** Visualisation of the reconstructed volumes for the *in silico* sample (a), which has different subvolumes with fibres preferentially oriented in different directions  $\theta_{fibre}$  (b). The orientation vector is visualized according to a color scheme (c) which maps the absolute value of its components  $[x,y,z]$  to the  $[R,G,B]$  values. Axial slices through the lower and upper part of the reconstructed sample acquired with the stairwise (d) and spiral (e) acquisition protocols are shown.  $n$  represents the number of turns. The color bars for the average scattering and scattering anisotropy are shown on the right.

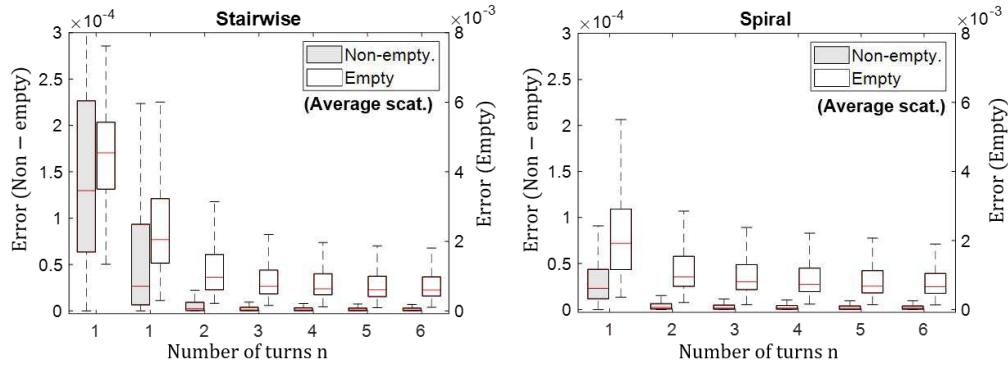
### 175 3.3 Validation sample

176 A validation sample (Fig. 6a) with a size of  $4 \times 4 \times 4 \text{ mm}^3$  as described in our previous publication<sup>16</sup> was used. The sample has  
 177 carbon fibres with a diameter of  $12 \mu\text{m}$  bundled and inserted into three different regions indicated as 1, 2, and 3. The projection  
 178 images were acquired with a parallel synchrotron monochromatic X-ray beam (17 keV, bandwidth of 2-3%) at the TOMCAT  
 179 beamline, Swiss Light Source, Paul Scherrer Institut. The beam size was  $14.3 \times 4.8 \text{ mm}^2$  and the effective FOV achieved with  
 180 vertically stitched scans was  $14.3 \times 12.7 \text{ mm}^2$ . The  $\pi$ -shift circular grating array had a unit cell period of  $P = 49.5 \mu\text{m}$  and a  
 181 fine grating period of  $g = 1.46 \mu\text{m}$  (Fig. 1b). A LuAG:Ce scintillator with a thickness of  $300 \mu\text{m}$  was used to convert incoming  
 182 X-rays to photons in the optical energy range compatible with the used camera and was placed at a distance  $L = 49.5 \text{ cm}$   
 183 (Fig. 1a) from the grating array. Visible light photons were delivered to the detector by a high numerical aperture 1x microscope  
 184 optics accepting a diagonal up to 40 mm. The in-house developed GigaFRoST<sup>27</sup> sCMOS detector with a sensor pixel size of  
 185  $11 \mu\text{m}$  was used. The fringe pattern in each unit cell was sampled with  $9 \times 9$  detector pixel windows. The exposure time for  
 186 each projection image was 10ms and projection images were acquired in a continuous manner.

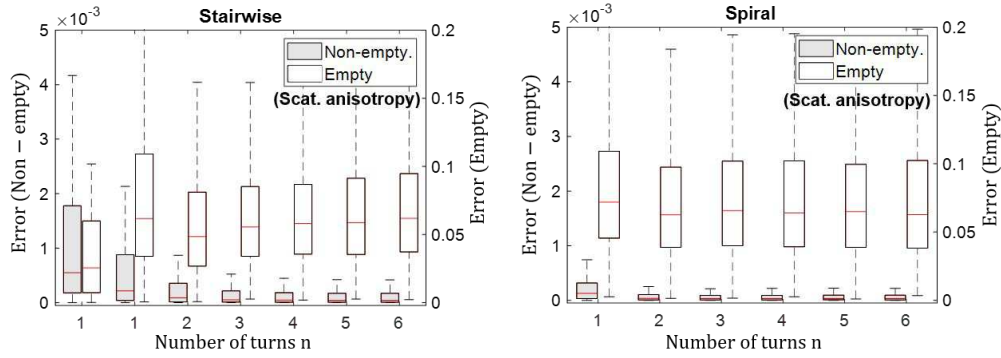
187 The reference reconstruction visualized in Fig. 6b was generated with the stairwise acquisition scheme with projection



(a) Inner product  $I$  of the orientation vectors



(b) Error  $E$  of the average scattering



(c) Error  $E$  of the scattering anisotropy

**Figure 5.** Quantitative assessment of the reconstruction accuracy for the *in silico* sample. Box plots of the inner product  $I$  for the different preferential orientations are shown in (a). The error  $E$  of the average scattering is shown in (b) and of the scattering anisotropy in (c). Note the separate axis scales of the non-empty and the empty volume.

188 images taken at 100 rotation and 46 tilt angles:  $\alpha = \{0^\circ, 3.6^\circ, \dots, 356.4^\circ\}$  and  $\beta = \{0^\circ, 1^\circ, \dots, 45^\circ\}$ . The reconstructed volume  
 189 was used as reference ("ground-truth") for the qualitative and quantitative comparison of the different acquisition protocols. For  
 190 the results for the stairwise acquisition scheme shown in Fig. 6c, the full reference dataset was uniformly sub sampled for the  
 191 desired  $n$  values so that always a total of 100 projection images was used for the reconstruction. For instance, 100 projection  
 192 images were taken at tilt angle  $\beta = 0^\circ$  for  $n = 1$ , and 33 projection images were taken at each tilt angle  $\beta = \{0^\circ, 23^\circ, 45^\circ\}$   
 193 for  $n = 3$ . For the spiral acquisition geometry, a total of 100 projection images homogeneously distributed along the spiral  
 194 trajectories with different  $n$  values, where  $\beta_{min} = 0^\circ$  and  $\beta_{max} = 45^\circ$ , were acquired and considered for the reconstruction  
 195 (Fig. 6d). A stitched scan was performed due to the limited beam height and the sample translation for three stitches caused a  
 196 few seconds of overhead. For the different geometries, the tensor reconstruction was performed following the method described  
 197 in 2.1, with a volume geometry of  $81 \times 81 \times 76$  voxels.

198 From the axial slices shown in Fig. 6b-6d, it is clear that the reconstruction with a fixed tilt angle of  $\beta = 0^\circ$  deviates the  
 199 most from the reference images. The reconstructions improved for  $\beta = 22.5^\circ$  or for spiral acquisition when  $n = 1$  although

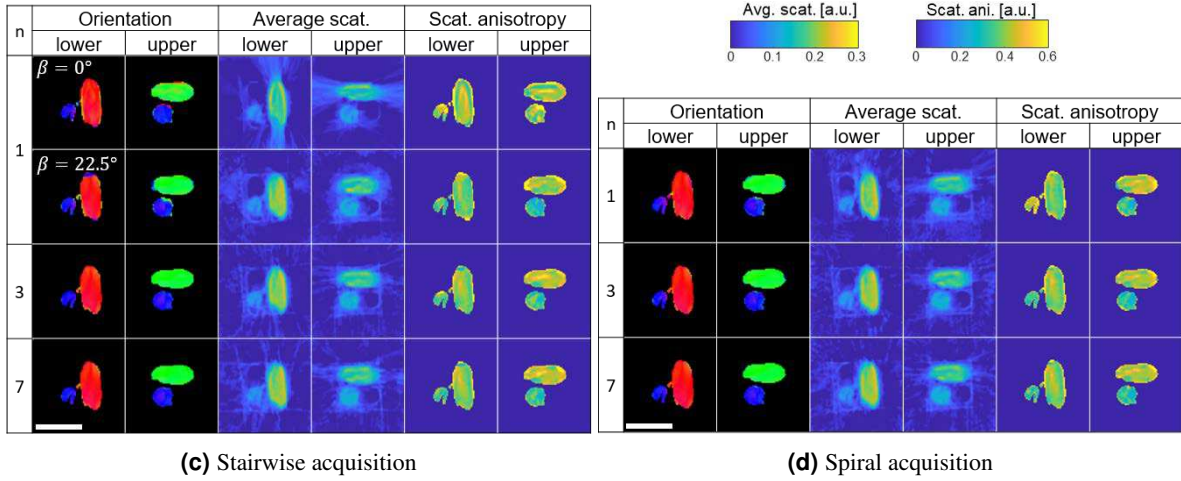
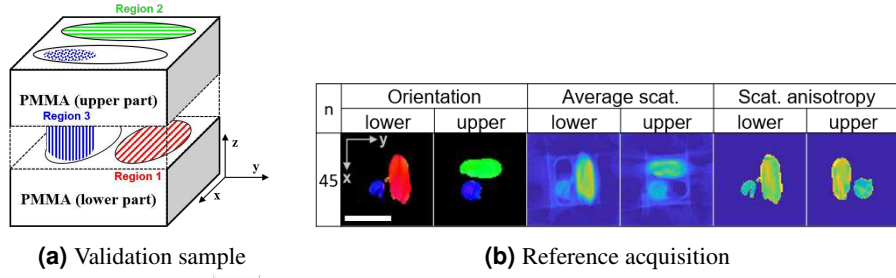


**Figure 6.** Visualisation of the reconstructed volumes for the validation sample. The validation sample (a) with three carbon fibre bundles oriented orthogonal to one another. Axial slices through the lower and the upper part of the validation sample reconstructed from the data acquired with the reference (b), the stairwise (c) and the spiral (d) acquisition protocols. Fibre orientation, average scattering and scattering anisotropy values are shown for each acquisition scheme. Scale bar: 4 mm

200 they still visually deviate from the reference. Only minor deviation from the reference is instead visually observable for all  
 201 other cases. These observations are qualitatively in agreement with the null space analysis and the simulation results shown in  
 202 the previous sections. In addition to the visual comparison of the reconstruction results, we have also performed a quantitative  
 203 analysis with the inner product  $I$  and the scalar error  $E$ . For the results evaluation (Fig. 7), voxels belonging to the 3 different  
 204 regions shown in Fig. 6a have been considered. The inner product  $I$  was calculated for each region defined as the group of  
 205 voxels in a box surrounding the region and the results are shown in Fig. 7a. We observe relatively more deviation from the  
 206 reference with a fixed tilt angle of  $\beta = 0^\circ$  compared to the other cases. Also, the deviation is larger for the region 1 and 2  
 207 where the fibres lie in the horizontal (x-y) plane. As projection views at tilt angles larger than  $0^\circ$  are added, the reconstruction  
 208 accuracy in the x-y plane increases. For  $n \geq 3$ , the reconstructed orientation is already close to the reference for both the  
 209 stairwise and spiral acquisition schemes. For the calculation of the error  $E$ , the reconstructed volume was subdivided in empty  
 210 and non-empty regions by applying a threshold to the average scattering. The group of voxels with an average scattering  
 211 signal higher than 30% of the maximum signal over the entire reference volume was defined as the non-empty region and  
 212 the group of voxels with a signal smaller than the defined threshold was defined as the empty region. For the pixels in both  
 213 regions, the error  $E$  was calculated and the box plots are shown in Fig. 7b, 7c. In general, the error  $E$  was largest when  $n = 1$   
 214 for the stairwise acquisition, whereas no major difference is observed for  $n \geq 3$ , in agreement with the analyses in the previous  
 215 sections. The error  $E$  for the scattering anisotropy in the empty regions was particularly large (Fig. 7c) as also observed in the  
 216 simulation study (Fig. 5c). We believe that this is because the scattering anisotropy is proportional to the square root of the  
 217 ratio of the variance to mean of the lengths of the principal axes of the scattering ellipsoid and is inherently more prone to  
 218 noise. In particular in background regions where the average scattering contribution is small or none and at sharp edges where  
 219 the scattering direction changes over a short distance, scattering anisotropy signals could appear artificially large. A mask  
 220 based on either the average scattering or the absorption is therefore necessary to properly visualize volumes with the scattering  
 221 anisotropy. The simplest type of such a mask sets all voxels with a value below a certain threshold to zero. A threshold based  
 222 mask was created from the average scattering information and applied to the scattering anisotropy visualisation in Fig. 6b-6d.

223 For the scattering anisotropy visualisation in the simulation study (Fig. 4d and 4e), all voxels outside the ground truth sample boundary were set to zero.

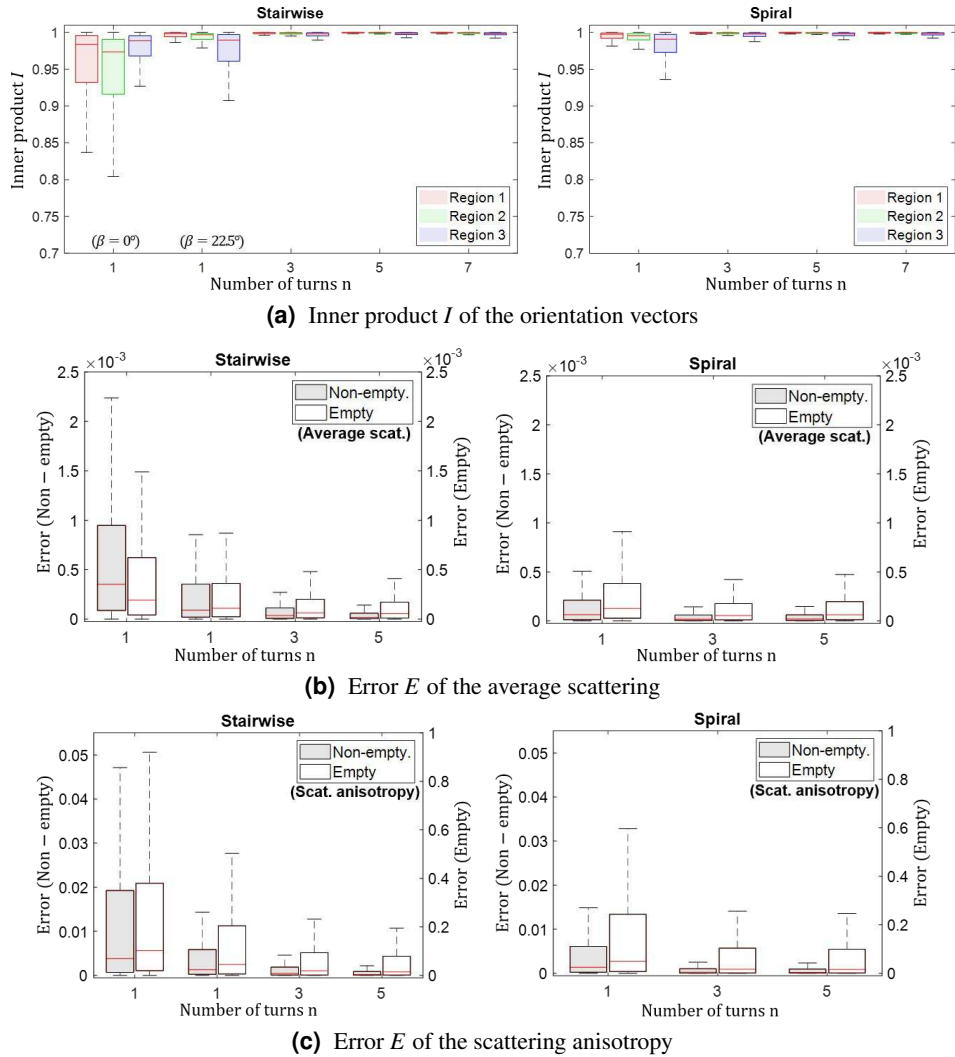


**Figure 7.** Quantitative assessment of the reconstruction accuracy for the validation sample. Box plots of the inner product  $I$  for the different preferential orientations (a). The error  $E$  of the average scattering is shown in (b) and of the scattering anisotropy in (c). Note the separate axis scales of the non-empty and the empty volume.

224

### 225 3.4 Fibre pellet assembly phantom

226 The fibre pellet phantom shown in Fig. 8 which is an assembly of different stick pellets composed of industrially relevant  
 227 fibre-reinforced materials was measured and analyzed. This assembly is a multi-material validation sample where the fibre or  
 228 tubular structures are aligned along the axial direction of each stick as can be seen in the Supplementary Fig. S1 online. The  
 229 experimental conditions were the same as in section 3.3 except that the projection images were acquired with 30keV. The  
 230 used high-aspect ratio circular grating array specific for 30keV was fabricated with an optimized deep reactive ion etching  
 231 process into a silicon substrate with a circular pattern mask generated by e-beam lithography<sup>20</sup>. This  $\pi$ -shift circular grating  
 232 array had the same dimension as the array used in the previous experiment but a different grating depth dictated by the chosen  
 233 energy. The beam size was  $11.6 \times 3.5 \text{ mm}^2$  and the effective FOV achieved with stitched scans was  $26.2 \times 22.5 \text{ mm}^2$ . The  
 234 scintillator-detector assembly was placed at a distance  $L = 74.1 \text{ cm}$  from the grating array. One hundred projection images  
 235 were acquired in a continuous manner and the exposure time for each projection image was 10 ms.

236 The sample was reconstructed from data acquired with the stairwise acquisition scheme with  $n = 1$  and  $n = 5$ . It was also  
 237 reconstructed from data acquired with a spiral acquisition protocol with  $n = 5$ . With all acquisition schemes used, it was possible  
 238 to recover, at least qualitatively, the expected fibre orientations as shown in Fig. 8d. In order to provide a comparison with the

239 measured data, an arbitrary projection angle was chosen at a tilted view of  $22.5^\circ$ . The measured and the forward projection  
 240 images for this angle are shown in Fig. 8e. The directional scattering signal (visibility reduction)  $V$  in the projection plane  
 241 was modelled with a cosine function  $V(\gamma) = a_0 + a_1 \cos(\gamma - \gamma_{main})^{15}$ . The three parameters  $a_0$ ,  $a_1$  and  $\gamma_{main}$  were extracted by  
 242 Fourier analysis.  $a_0$  represents the average scattering and the degree of anisotropy is computed as the ratio  $a_1/a_0$ .  $\gamma_{main}$  is the  
 243 main direction of the underlying structure. These three parameters are coded with the HSV coloring scheme: H as the main  
 244 orientation, S as the degree of scattering anisotropy, V as the average scattering. The color coded projection images are shown  
 245 in Fig. 8e where H and S are mapped by the color wheel. V appears as the brightness of the pixel (dark as V approaches 0,  
 246 bright as V approaches 1). The acquisition protocol with  $n = 1$  ( $\beta = 0^\circ$ ) gave a forward projection image which deviated the  
 247 most from the measured projection whereas the other two protocols with  $n = 5$  gave much similar projection images. These  
 experimental results are in agreement with the previous sections.

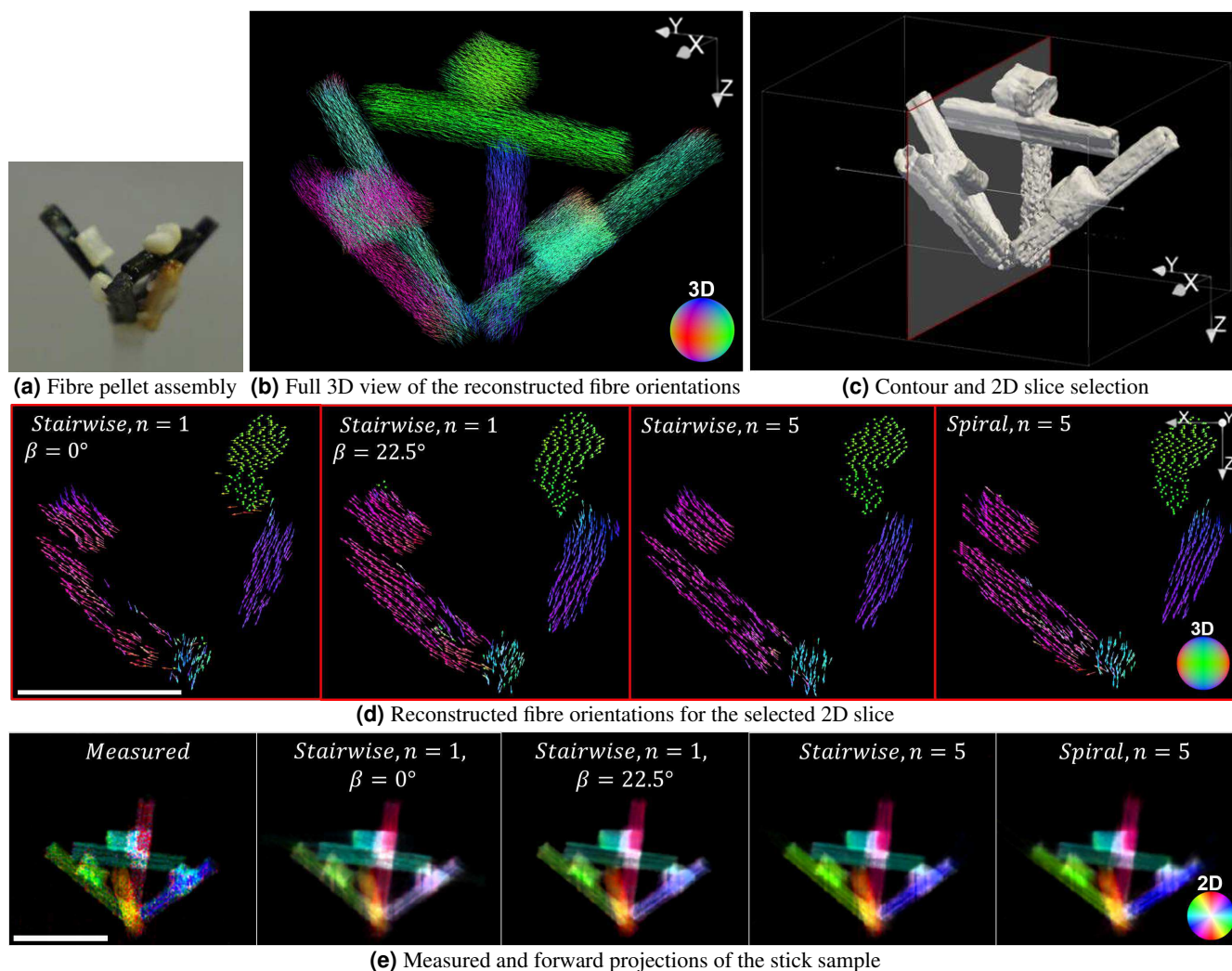


**Figure 8.** Fibre pellet phantom analysis - (a) The sample is composed of carbon (black) and glass fibre (white) material as well as wood (brown). (b) Full 3D view of the reconstructed fibre orientations (stairwise,  $n = 5$ ). (c) Contour image based on the average scattering signal. (d) Reconstructed fibre orientation for the 2D slice shown in (c) (subsampled by a factor of 5 for visualisation). The 3D color ball maps the 3D fibre orientation. (e) Measured and forward projection images at an arbitrary angle. The 2D color wheel maps the fibre orientations projected onto the 2D detector plane. Scale bar: 1 cm

248

## 249 4 Discussion

250 The *in-silico* as well as the experimental studies show that simple protocols compatible with fast acquisition schemes are  
 251 possible. In general for higher accuracy the number of turns  $n$  has to be at least  $\geq 1$ . If the acquisition speed needs though  
 252 to be maximized, for instance for studying fast dynamic processes, the spiral acquisition protocol with  $n = 1$  can provide

sufficient accuracy for many applications. If even further simplification is unavoidable, for example if using complex sample environments for which fast simultaneous rotation around 2 axes is cumbersome, acquisition at a fixed tilt angle is also a viable solution. This fixed tilt angle should though be chosen carefully and in most cases the trivial selection of  $\beta = 0^\circ$  is not the optimal choice as shown by the null space analysis and the different reconstruction studies. A fixed tilt angle of  $\beta = 22.5^\circ$  provides superior results compared to the trivial choice and similar accuracy to the spiral protocol with  $n = 1$ . Even though a system with 2 axes of rotation is in principle required also for the fixed tilt angle case to ensure flexibility in the selection of  $\beta$ , rotation around a single axis during data acquisition strongly simplifies all synchronisation aspects, not irrelevant at high speed, potentially leading to less uncertainties in the reconstruction process of the final volume. For specific applications, e.g. to increase the stability of the setup, a single rotation stage firmly mounted with the rotation axis at a defined angle with respect to the beam can also be an option to consider.

The advantage of  $n$  at least  $> 1$  by a constant number of projection is clear and a relevant observation was made by a previous scanning SAXS based tensor tomography study that the reconstruction accuracy is more related to having a sufficient number of turns  $n$  than having a larger total number of projections<sup>24</sup>. For the reconstruction volume sizes in our experimental studies, 100 projections lead to undersampled tomographic datasets; we have nonetheless decided to use such a small number of projections with small  $n$  values in the presented experiments to effectively push the acquisition speed with fast tensor tomography applications in mind. The effect of further reducing the number of projections leading to extremely sparse datasets in conjunction with the proposed acquisition protocols needs though to be investigated but is beyond the scope of this study.

A direct quantitative comparison of our method to existing tensor tomography methods of all involved aspects is not straightforward and beyond the scope of this work. Our method in general has a larger voxel size compared to the existing methods and thus it may yield lower spatial resolution with the absorption contrast. However, microstructure is indirectly revealed by the small-angle scattering signal in scattering tensor tomography rather than directly resolved by detector pixels. Thus, spatial resolution is often not of the main importance for tensor tomography and the effective spatial resolution is rarely reported in published studies. Scans are rather optimized for different purposes and different samples, and different sources are used. We still would like to note that it is in general clear that the large acquisition overhead intrinsic in the scanning SAXS geometry limits this method to small samples and makes it unsuitable for imaging industrially relevant large volumes or dynamic processes. On the other hand, reported grating interferometric studies with linear gratings are almost exclusively performed on conventional lab-based sources. Therefore, it is meaningless to directly compare the scan time because the exposure time for a single radiographic projection is significantly longer than at a synchrotron. Nevertheless, the need of rather complex trajectories and phase stepping with linear gratings causes frequent discontinuities in the acquisition process increasing the overall overhead even if this technique would be used with a higher flux source.

With our method at synchrotron facilities, the exposure time for each single radiographic projection is usually in the order of a few to a few tens ms. Using an  $n = 1$  protocol with 100 projections continuously acquired, mostly sufficient for the experimental configurations used in this study, one full omni-directional scattering tensor tomographic volume covering e.g.  $16 \times 16 \times 4 \text{ mm}^3 = 1 \text{ cm}^3$ , with a spatial resolution in the order of 50 to  $100 \mu\text{m}$  can be acquired in less than 1 s. This means that macroscopic, statistically relevant samples (e.g.  $10 \text{ cm}^3$ ) can be routinely investigated in a matter of minutes even taking into account the overhead related to sample movements for stitched scan. Alternatively, if a dynamic process is of interest, it is possible to follow the same evolving volume through time.

## 5 Conclusion

In this study, comparative analyses were presented for simple acquisition protocols optimally suited for rapid scattering tensor tomography. First, the null space was significantly reduced by substituting conventional linear with circular gratings already when the tilt angles or the number of spiral turns  $n$  were just 1. This first mathematical evidence highlighted the potential of using a circular grating array for fast scattering tensor tomography with simple acquisition geometries with a fairly small  $n$ . Second, simulation studies with an *in silico* sample showed that the reconstructed volumes were already close to the ground truth with  $n \leq 3$ , regardless of the used acquisition protocol. Lastly, experimental studies provided results that were in agreement with the null space analysis as well as with the simulation results demonstrating the robustness of the technique with respect to the unavoidable experimental uncertainties.

We conclude that, with a circular grating array, the suggested simple acquisition schemes with a fairly small number of turns  $n$  are inherently sufficient in providing directional scattering information for scattering tensor tomography. Thus, the proposed acquisition protocols build the basis towards rapid inspection and/or time-resolved X-ray scattering tensor tomography in the near future. In principle, the proposed acquisition protocols are compatible with and can be easily transferable to X-ray tube setups and the range of applications can be expanded to industrially more relevant problems. In addition, the presented framework of the null space analysis will be useful to assess and optimize in advance an arbitrary acquisition protocol for X-ray scattering tensor tomography. Even though this work is based on a circular grating array, the proposed acquisition protocols can actually to be also directly transferred to any tensor tomography modality with omnidirectional scattering sensitivity such as

307 speckle pattern, scanning SAXS, and omnidirectional simultaneous reciprocal and real space imaging based methods.

## 308 **6 Data availability**

309 The datasets generated and analysed during the current study are available from the corresponding author on reasonable request.

## 310 **References**

- 311 **1.** Fratzl, P. Collagen: Structure and Mechanics, an Introduction. In Fratzl, P. (ed.) *Collagen*, 1–13, DOI: [10.1007/](https://doi.org/10.1007/978-0-387-73906-9_{_}1)  
312 [978-0-387-73906-9\\_{\\_}1](https://doi.org/10.1007/978-0-387-73906-9_{_}1) (Springer US, Boston, MA, 2008).
- 313 **2.** Meyers, M. A., McKittrick, J. & Chen, P.-Y. Structural Biological Materials: Critical Mechanics-Materials Connections.  
314 *Science* **339**, 773–779, DOI: [10.1126/science.1220854](https://doi.org/10.1126/science.1220854) (2013).
- 315 **3.** Jbabdi, S., Sotiropoulos, S. N., Haber, S. N., Van Essen, D. C. & Behrens, T. E. Measuring macroscopic brain connections  
316 in vivo. *Nat. Neurosci.* **18**, 1546–1555, DOI: [10.1038/nn.4134](https://doi.org/10.1038/nn.4134) (2015).
- 317 **4.** Byron Pipes, R., McCullough, R. L. & Taggart, D. G. Behavior of discontinuous fiber composites: Fiber orientation.  
318 *Polym. Compos.* **3**, 34–39, DOI: [10.1002/pc.750030107](https://doi.org/10.1002/pc.750030107) (1982).
- 319 **5.** Abbasi, S., Carreau, P. J. & Derdouri, A. Flow induced orientation of multiwalled carbon nanotubes in polycarbonate  
320 nanocomposites: Rheology, conductivity and mechanical properties. *Polymer* DOI: [10.1016/j.polymer.2009.12.041](https://doi.org/10.1016/j.polymer.2009.12.041) (2010).
- 321 **6.** Martin, J. J., Fiore, B. E. & Erb, R. M. Designing bioinspired composite reinforcement architectures via 3D magnetic  
322 printing. *Nat. Commun.* **6**, 8641, DOI: [10.1038/ncomms9641](https://doi.org/10.1038/ncomms9641) (2015).
- 323 **7.** Yashiro, W., Terui, Y., Kawabata, K. & Momose, A. On the origin of visibility contrast in x-ray Talbot interferometry. *Opt.*  
324 *Express* **18**, 16890, DOI: [10.1364/OE.18.016890](https://doi.org/10.1364/OE.18.016890) (2010).
- 325 **8.** Lynch, S. K. *et al.* Interpretation of dark-field contrast and particle-size selectivity in grating interferometers. *Appl. Opt.*  
326 **50**, 4310, DOI: [10.1364/AO.50.004310](https://doi.org/10.1364/AO.50.004310) (2011).
- 327 **9.** Strobl, M. General solution for quantitative dark-field contrast imaging with grating interferometers. *Sci. Reports* **4**, 7243,  
328 DOI: [10.1038/srep07243](https://doi.org/10.1038/srep07243) (2015).
- 329 **10.** Liebi, M. *et al.* Nanostructure surveys of macroscopic specimens by small-angle scattering tensor tomography. *Nature*  
330 **527**, 349–352, DOI: [10.1038/nature16056](https://doi.org/10.1038/nature16056) (2015).
- 331 **11.** Schaff, F. *et al.* Six-dimensional real and reciprocal space small-angle X-ray scattering tomography. *Nature* **527**, 353–356,  
332 DOI: [10.1038/nature16060](https://doi.org/10.1038/nature16060) (2015).
- 333 **12.** Jensen, T. H. *et al.* Directional x-ray dark-field imaging of strongly ordered systems. *Phys. Rev. B* **82**, 214103, DOI:  
334 [10.1103/PhysRevB.82.214103](https://doi.org/10.1103/PhysRevB.82.214103) (2010).
- 335 **13.** Sharma, Y., Schaff, F., Wiczorek, M., Pfeiffer, F. & Lasser, T. Design of Acquisition Schemes and Setup Geometry for  
336 Anisotropic X-ray Dark-Field Tomography (AXDT). *Sci. Reports* **7**, 3195, DOI: [10.1038/s41598-017-03329-0](https://doi.org/10.1038/s41598-017-03329-0) (2017).
- 337 **14.** Kagias, M., Wang, Z., Villanueva-Perez, P., Jefimovs, K. & Stampanoni, M. 2D-Omnidirectional Hard-X-Ray Scattering  
338 Sensitivity in a Single Shot. *Phys. Rev. Lett.* **116**, 093902, DOI: [10.1103/PhysRevLett.116.093902](https://doi.org/10.1103/PhysRevLett.116.093902) (2016).
- 339 **15.** Kagias, M. *et al.* Diffractive small angle X-ray scattering imaging for anisotropic structures. *Nat. Commun.* **10**, 5130, DOI:  
340 [10.1038/s41467-019-12635-2](https://doi.org/10.1038/s41467-019-12635-2) (2019).
- 341 **16.** Kim, J., Kagias, M., Marone, F. & Stampanoni, M. X-ray scattering tensor tomography with circular gratings. *Appl. Phys.*  
342 *Lett.* **116**, 134102, DOI: [10.1063/1.5145361](https://doi.org/10.1063/1.5145361) (2020).
- 343 **17.** Malecki, A. *et al.* X-ray tensor tomography. *EPL (Europhysics Lett.)* **105**, 38002, DOI: [10.1209/0295-5075/105/38002](https://doi.org/10.1209/0295-5075/105/38002)  
344 (2014).
- 345 **18.** Zanette, I. *et al.* Speckle-based x-ray phase-contrast and dark-field imaging with a laboratory source. *Phys. Rev. Lett.* DOI:  
346 [10.1103/PhysRevLett.112.253903](https://doi.org/10.1103/PhysRevLett.112.253903) (2014).
- 347 **19.** Dreier, E. S. *et al.* Single-shot, omni-directional x-ray scattering imaging with a laboratory source and single-photon  
348 localization. *Opt. Lett.* DOI: [10.1364/ol.381420](https://doi.org/10.1364/ol.381420) (2020).
- 349 **20.** Shi, Z., Jefimovs, K., Romano, L. & Stampanoni, M. Towards the Fabrication of High-Aspect-Ratio Silicon Gratings by  
350 Deep Reactive Ion Etching. *Micromachines* **11**, 864, DOI: [10.3390/mi11090864](https://doi.org/10.3390/mi11090864) (2020).
- 351 **21.** Basser, P. J. & Pierpaoli, C. Microstructural and physiological features of tissues elucidated by quantitative-diffusion-tensor  
352 MRI. *J. Magn. Reson.* **213**, 560–570, DOI: [10.1016/j.jmr.2011.09.022](https://doi.org/10.1016/j.jmr.2011.09.022) (2011).

- 353 **22.** Vogel, J. *et al.* Constrained X-ray tensor tomography reconstruction. *Opt. Express* **23**, 15134, DOI: [10.1364/OE.23.015134](https://doi.org/10.1364/OE.23.015134)  
354 (2015).
- 355 **23.** Kagias, M., Wang, Z., Lovric, G., Jefimovs, K. & Stampanoni, M. Simultaneous Reciprocal and Real Space X-Ray  
356 Imaging of Time-Evolving Systems. *Phys. Rev. Appl.* **10**, 1, DOI: [10.1103/PhysRevApplied.15.044038](https://doi.org/10.1103/PhysRevApplied.15.044038) (2021).
- 357 **24.** Liebi, M. *et al.* Small-angle X-ray scattering tensor tomography: Model of the three-dimensional reciprocal-space map,  
358 reconstruction algorithm and angular sampling requirements. *Acta Crystallogr. Sect. A: Foundations Adv.* **74**, 12–24, DOI:  
359 [10.1107/S205327331701614X](https://doi.org/10.1107/S205327331701614X) (2018).
- 360 **25.** Zeng, G. L. & Gullberg, G. T. Null-space function estimation for the interior problem. *Phys. Medicine Biol.* **57**, 1873–1887,  
361 DOI: [10.1088/0031-9155/57/7/1873](https://doi.org/10.1088/0031-9155/57/7/1873) (2012).
- 362 **26.** Chabior, M. *et al.* Signal-to-noise ratio in x ray dark-field imaging using a grating interferometer. In *Journal of Applied*  
363 *Physics*, DOI: [10.1063/1.3630051](https://doi.org/10.1063/1.3630051) (2011).
- 364 **27.** Mokso, R. *et al.* GigaFRoST: the gigabit fast readout system for tomography. *J. Synchrotron Radiat.* **24**, 1250–1259, DOI:  
365 [10.1107/S1600577517013522](https://doi.org/10.1107/S1600577517013522) (2017).

## 366 **Acknowledgments**

367 This work received funding from the EU Horizon 2020 Marie Skłodowska-Curie grant 765604 (MUMMERING) and EU-  
368 ROSTARS INFORMAT E! 11060. The experiments were performed at the TOMCAT beamline, Swiss Light Source (SLS),  
369 Paul Scherrer Institut (PSI), Switzerland. We thank the SLS cSAXS beamline for allowing us to modify and use their sample  
370 stage. We thank Xnovo Technology ApS, Denmark for providing the fibre pellet phantom.

## 371 **Author contributions statement**

372 J.K. conceived and conducted the nullspace and the simulation studies. J.K., M.K., and F.M. conceived and conducted the  
373 experiments. J.K. analysed and visualised the results. M.K and Z.S. fabricated the gratings. M.K., F.M. and M.S. conceived the  
374 MUMMERING project providing the basis for this work. J.K. wrote the manuscript with contribution from all co-authors.

## 375 **Additional information**

376 **Competing interests:** The authors declare no competing interests.

# Figures

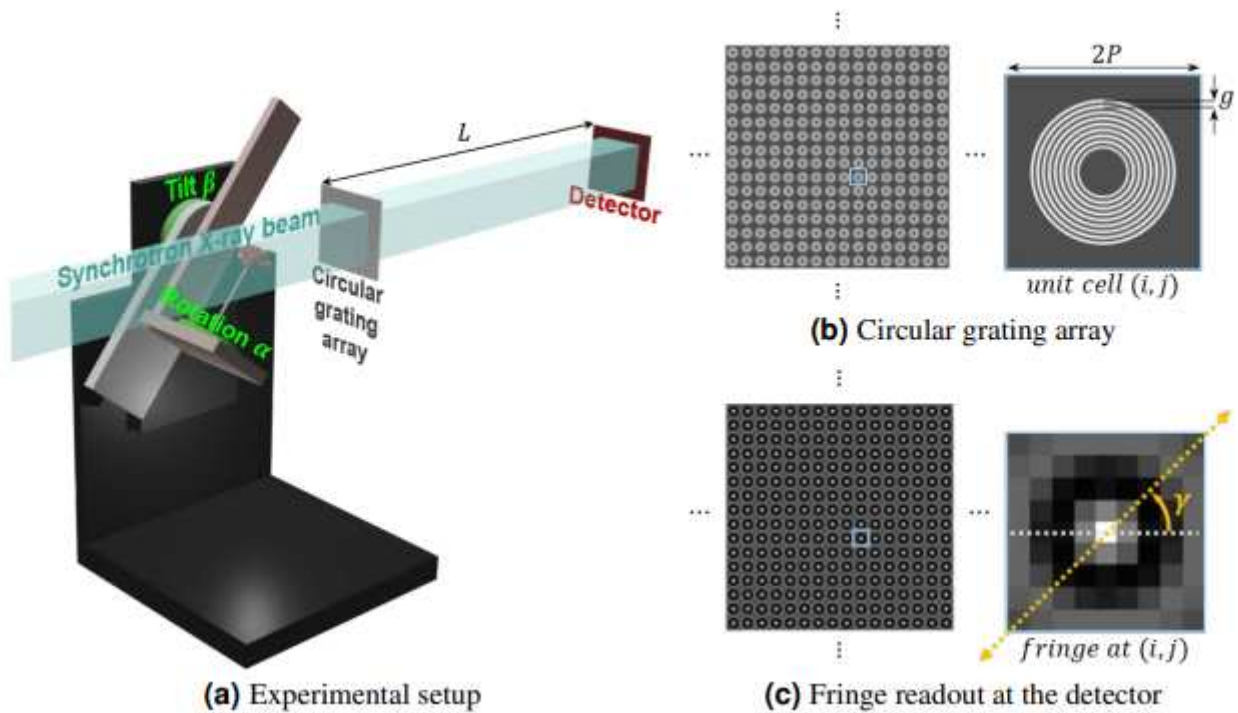
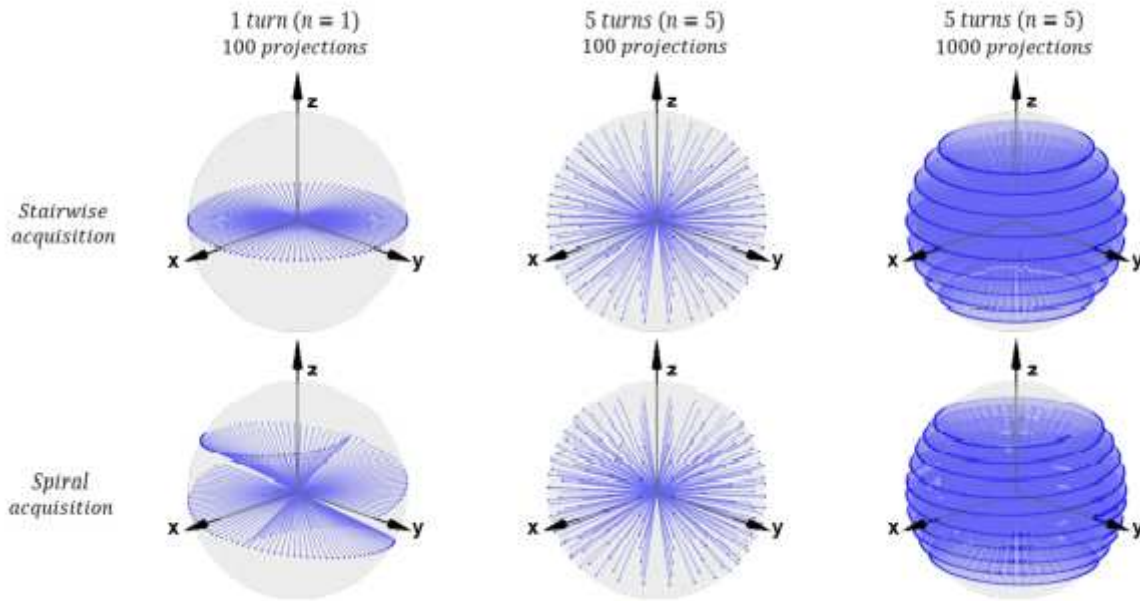


Figure 1

Experimental setup for X-ray scattering tensor tomography with circular gratings. An overview of the setup is shown in (a). The rotation motor revolves  $\alpha$  degrees and the rotation axis can be tilted  $\beta$  degrees. The circular grating array (b) is composed of unit cells where  $P$  is half the unit cell size and  $g$  is the period of the fine grating lines. It is placed near the sample at a distance  $L = Pg/2\lambda$  from the detector. A circular fringe (c) is formed at the detector where the 2D directional scattering signal is extracted by measuring the visibility reduction along the radial profile at an angle  $-90^\circ \leq \gamma < 90^\circ$ .



**Figure 2**

Beam enter/exit trajectories for stairwise and spiral acquisition schemes from the sample's point of view. The number of turns  $n$  and the total number of projections are indicated on top of the plots. The tilt angle  $\beta$  for the shown stairwise trajectory with  $n = 1$  is  $0^\circ$  but it can be chosen to be any angle between  $0^\circ$  and  $45^\circ$ .

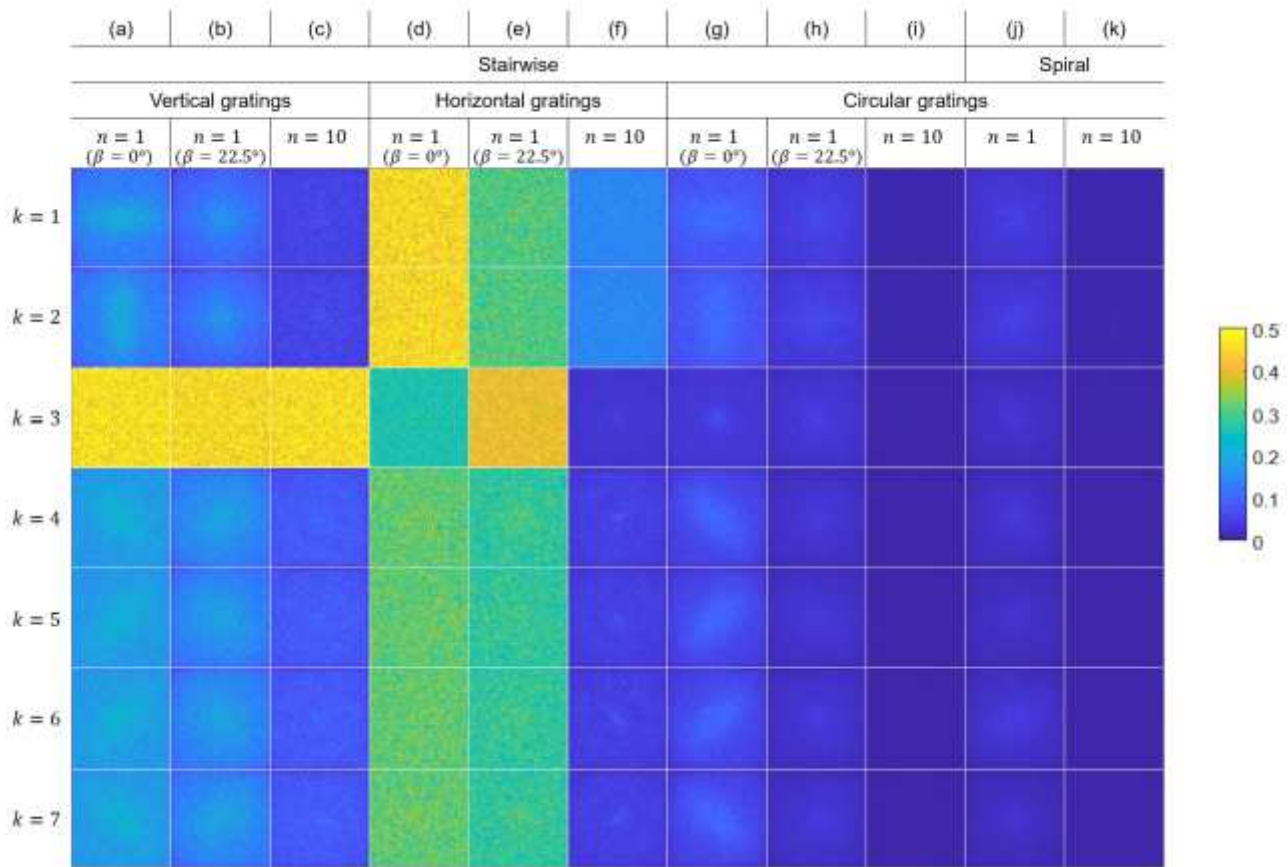


**Figure 3**

Visualisation of the computed null space for different scattering sampling directions  $k$ . The null space was computed for different acquisition geometries: stairwise and spiral acquisition; different grating types: vertically aligned linear gratings, horizontally aligned linear gratings, and circular gratings; different number of turns  $n$ .  $\beta$  indicates the tilt angle. High values in null space for scattering component  $k$  indicate that the acquisition protocol provides large uncertainties in the reconstruction for that component.

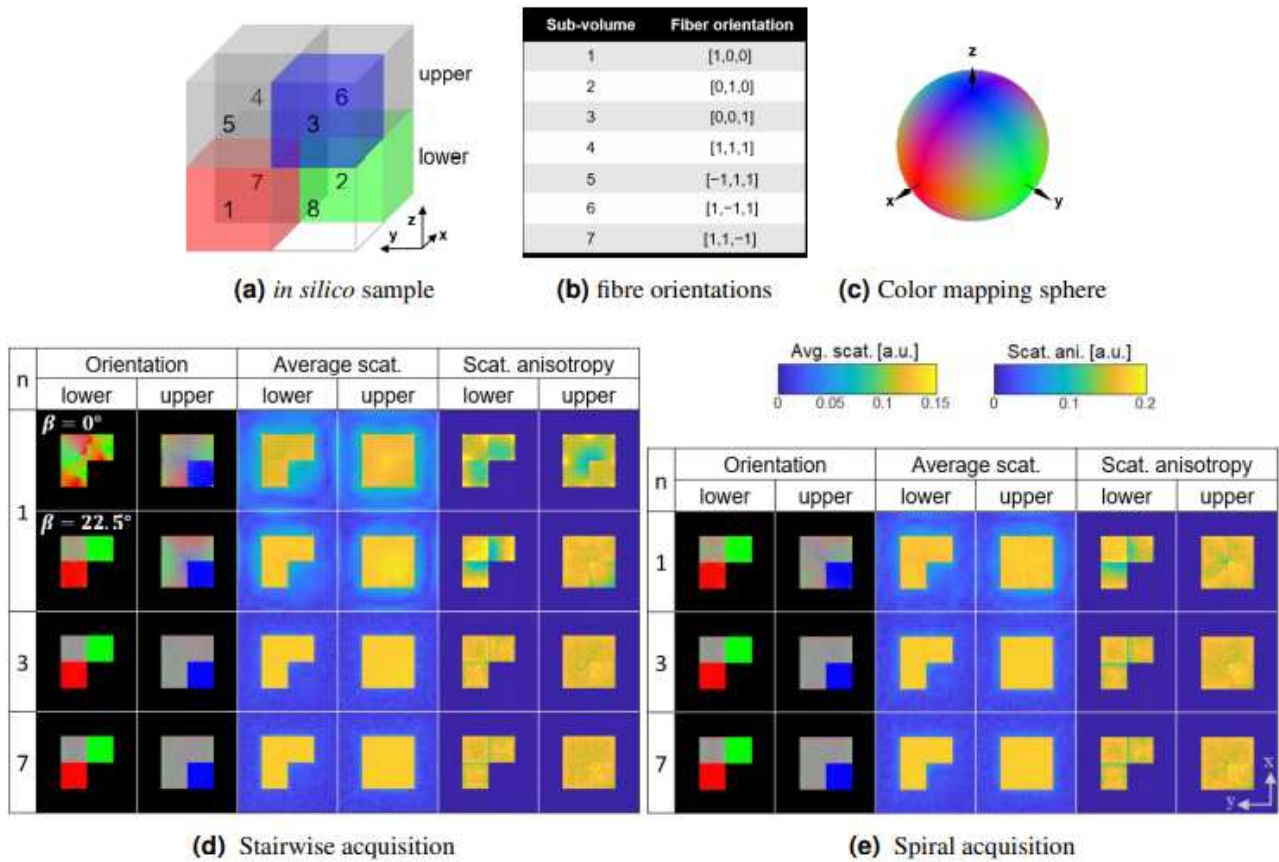
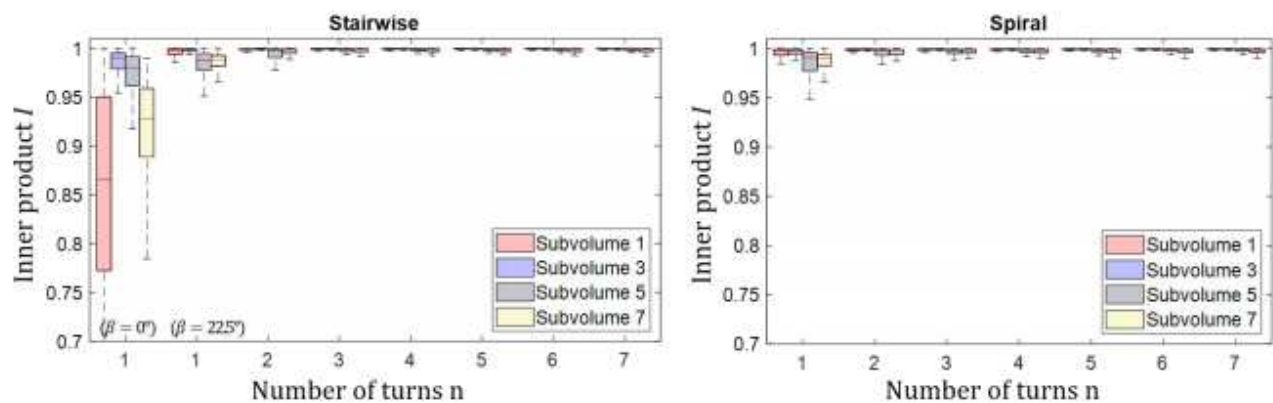
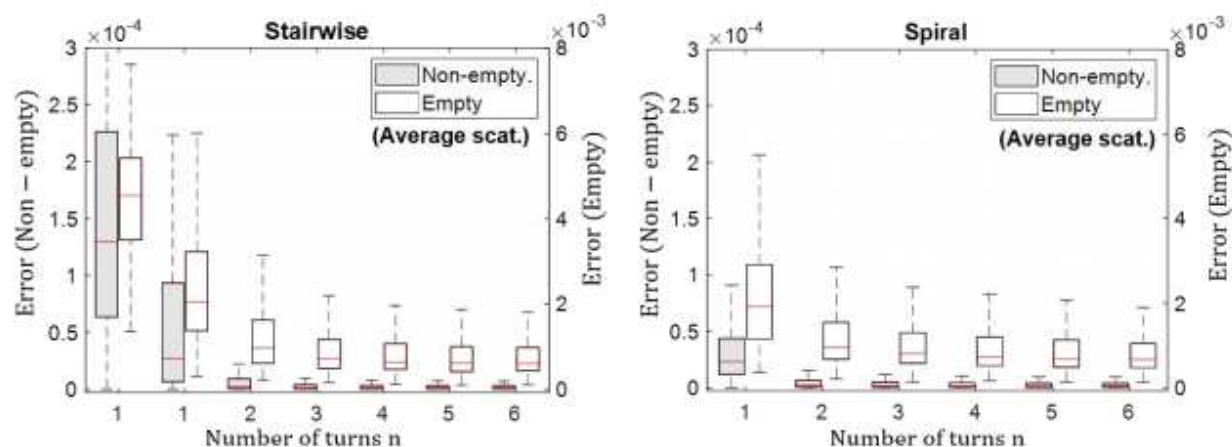


**Figure 4**

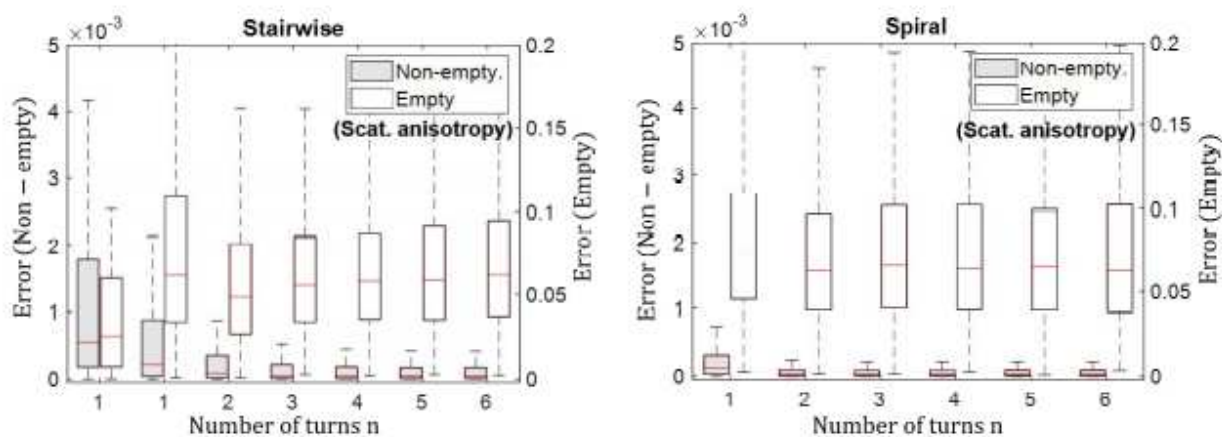
Visualisation of the reconstructed volumes for the in silico sample (a), which has different subvolumes with fibres preferentially oriented in different directions of fibre (b). The orientation vector is visualized according to a color scheme (c) which maps the absolute value of its components  $[x,y,z]$  to the  $[R,G,B]$  values. Axial slices through the lower and upper part of the reconstructed sample acquired with the stairwise (d) and spiral (e) acquisition protocols are shown.  $n$  represents the number of turns. The color bars for the average scattering and scattering anisotropy are shown on the right.



(a) Inner product  $I$  of the orientation vectors



(b) Error  $E$  of the average scattering



(c) Error  $E$  of the scattering anisotropy

Figure 5

Quantitative assessment of the reconstruction accuracy for the in silico sample. Box plots of the inner product  $I$  for the different preferential orientations are shown in (a). The error  $E$  of the average scattering is shown in (b) and of the scattering anisotropy in (c). Note the separate axis scales of the non-empty and the empty volume.

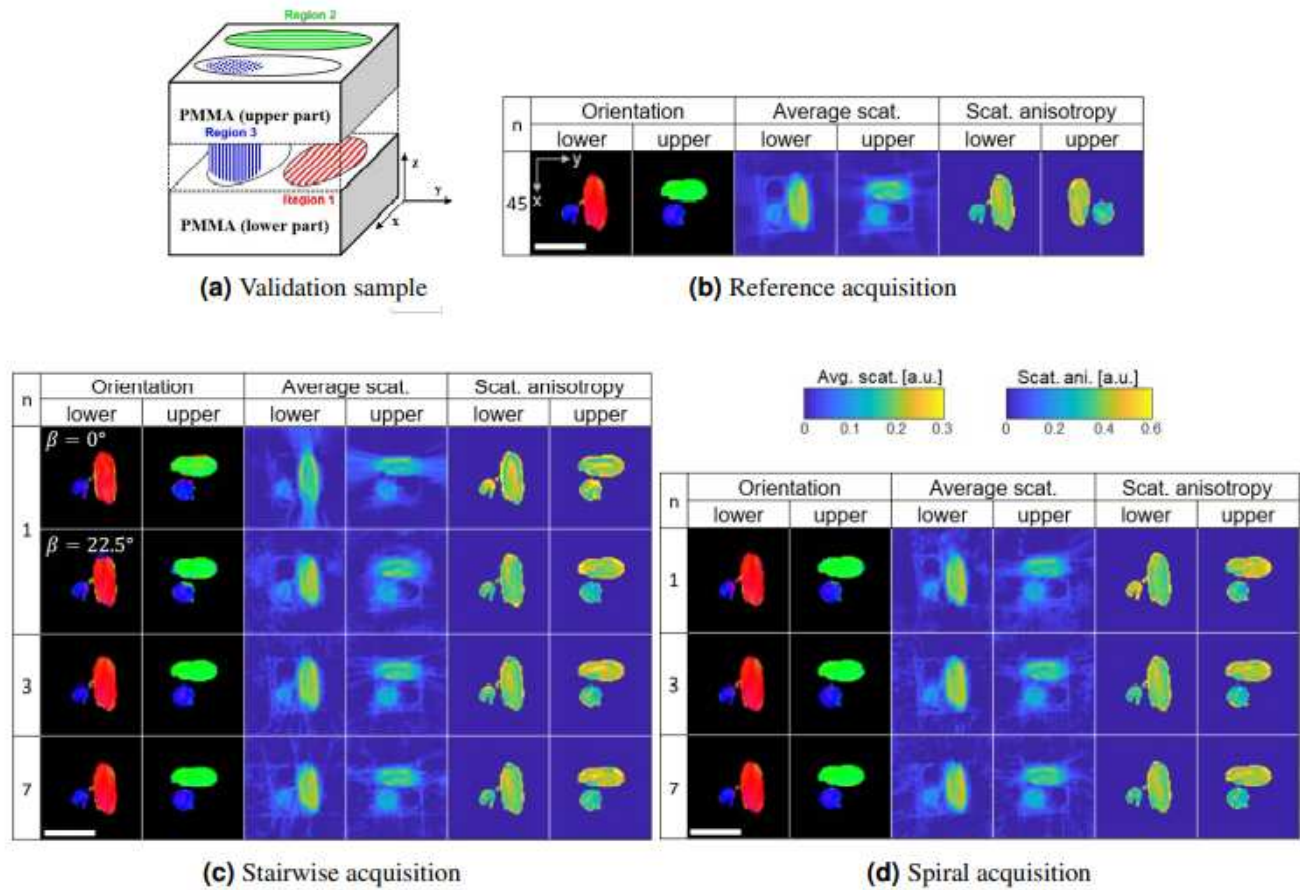
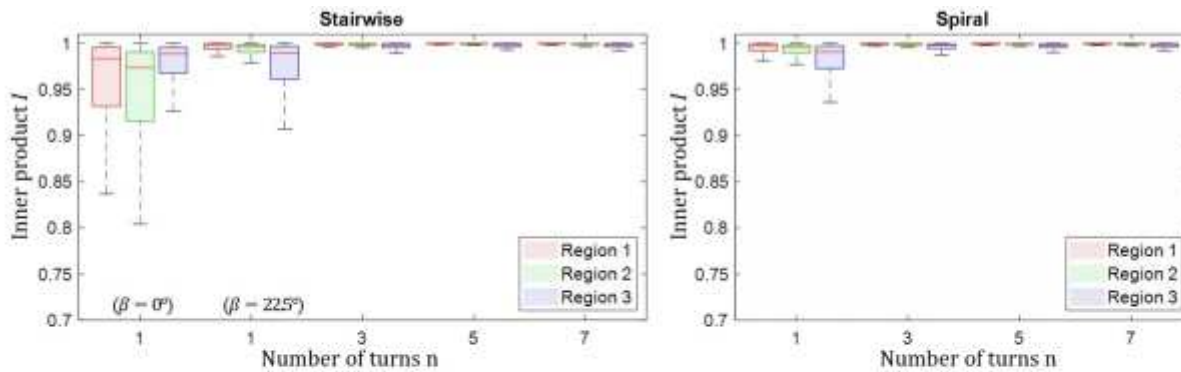
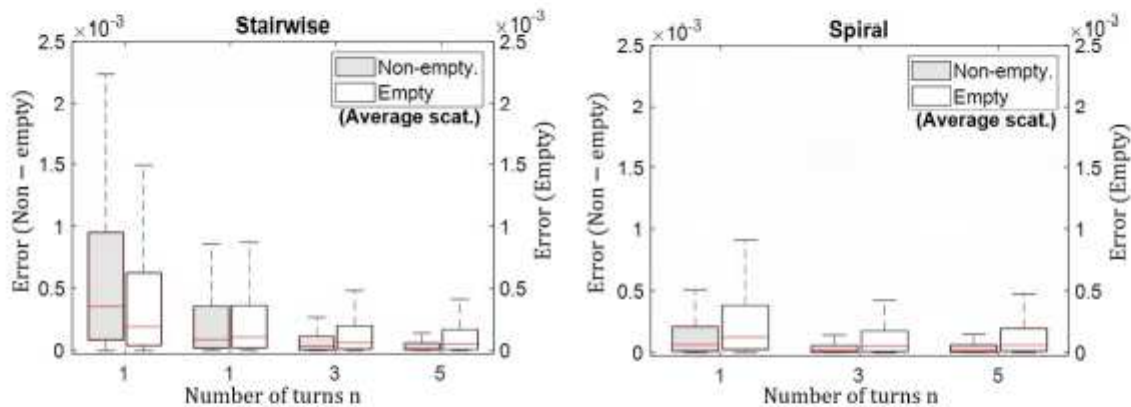


**Figure 6**

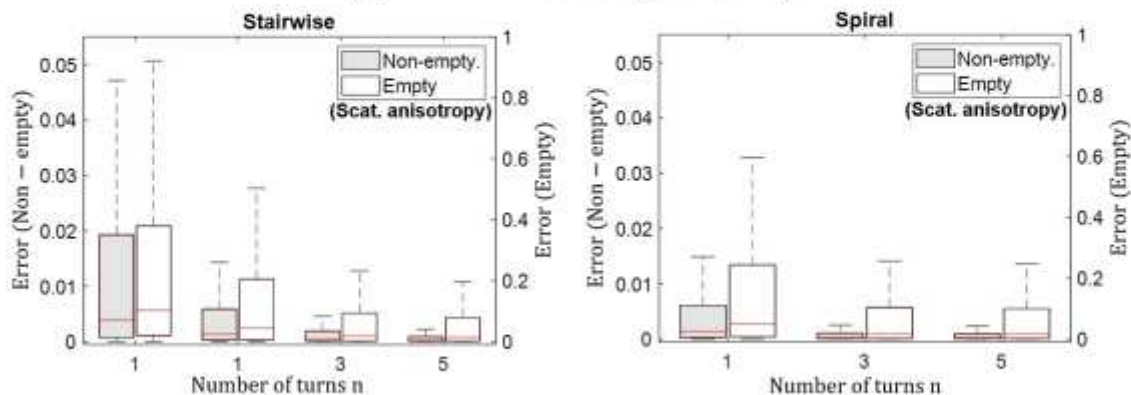
Visualisation of the reconstructed volumes for the validation sample. The validation sample (a) with three carbon fibre bundles oriented orthogonal to one another. Axial slices through the lower and the upper part of the validation sample reconstructed from the data acquired with the reference (b), the stairwise (c) and the spiral (d) acquisition protocols. Fibre orientation, average scattering and scattering anisotropy values are shown for each acquisition scheme. Scale bar: 4 mm



(a) Inner product  $I$  of the orientation vectors



(b) Error  $E$  of the average scattering



(c) Error  $E$  of the scattering anisotropy

Figure 7

Quantitative assessment of the reconstruction accuracy for the validation sample. Box plots of the inner product  $I$  for the different preferential orientations (a). The error  $E$  of the average scattering is shown in (b) and of the scattering anisotropy in (c). Note the separate axis scales of the non-empty and the empty volume.

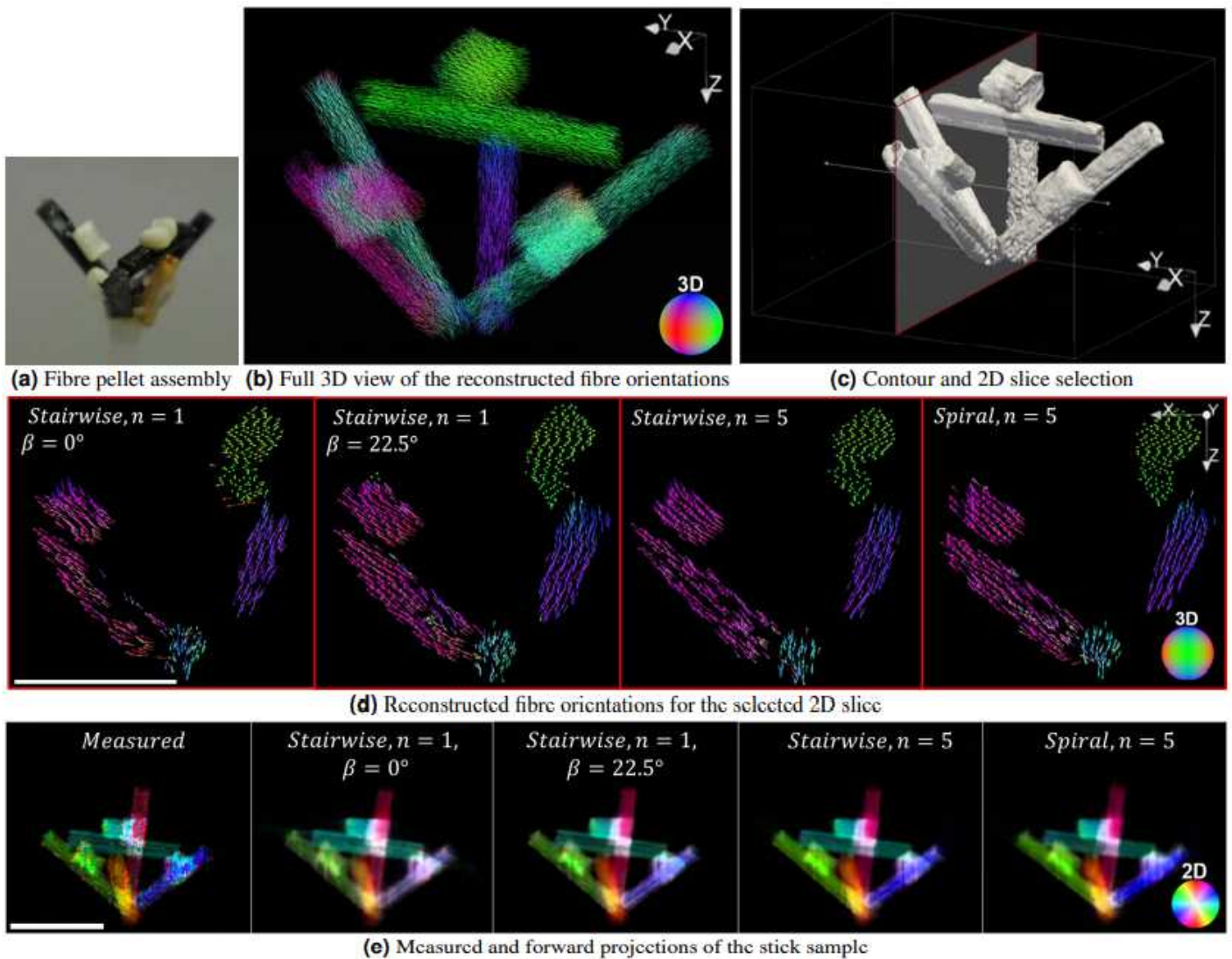


**Figure 8**

Fibre pellet phantom analysis - (a) The sample is composed of carbon (black) and glass fibre (white) material as well as wood (brown). (b) Full 3D view of the reconstructed fibre orientations (stairwise,  $n = 5$ ). (c) Contour image based on the average scattering signal. (d) Reconstructed fibre orientation for the 2D slice shown in (c) (subsamped by a factor of 5 for visualisation). The 3D color ball maps the 3D fibre orientation. (e) Measured and forward projection images at an arbitrary angle. The 2D color wheel maps the fibre orientations projected onto the 2D detector plane. Scale bar: 1 cm

## Supplementary Files

This is a list of supplementary files associated with this preprint. Click to download.

- [FastacquisitionprotocolforXrayscatteringtensortomographysupplementary.pdf](#)